PAPER • **OPEN ACCESS**

4D direct ink writing of body temperature-responsive triple-shape memory scaffolds for bone tissue engineering

To cite this article: Nasim Sabahi *et al* 2026 *Biofabrication* **18** 035035

Biofabrication

OPEN ACCESS

RECEIVED
15 February 2026

REVISED
23 June 2026

ACCEPTED FOR PUBLICATION
14 July 2026

PUBLISHED
27 July 2026

PAPER

4D direct ink writing of body temperature-responsive triple-shape memory scaffolds for bone tissue engineering

Nasim Sabahi[1], Iman Roohani[2], Kristopher A Kilian[3], Chun H Wang[1] and Xiaopeng Li[1,*]

[1] School of Mechanical and Manufacturing Engineering, The University of New South Wales (UNSW Sydney), Sydney 2052, NSW, Australia
[2] School of Biomedical Engineering, University of Technology, Sydney 2007, NSW, Australia
[3] School of Materials Science and Engineering, Australian Centre for NanoMedicine, The University of New South Wales (UNSW Sydney), Sydney 2052, NSW, Australia
[*] Author to whom any correspondence should be addressed.

E-mail: xiaopeng.li@unsw.edu.au

Keywords: 4D printing, direct ink writing (DIW), triple-shape memory polymer, smart scaffold, bone tissue engineering

Supplementary material for this article is available online

Abstract

Four dimensional printing of shape memory polymers (SMPs) holds significant promise for addressing irregular bone defects. The incorporation of SMPs with the ability to adopt multiple shapes greatly enhances the performance of 4D-printed scaffolds. These smart scaffolds not only provide crucial structural support but also actively interact with cells to promote and enhance regenerative processes. In this study, we successfully developed novel triple-SMPs with two distinct transition temperatures ($T_g = 34$ °C and $T_m = 56$ °C). By melt blending biocompatible thermoplastics, including polycaprolactone, thermoplastic polyurethane, and Poly (lactic-co-glycolic acid) (PLGA), at different weight ratios, we achieved over 90% shape recovery ratios during two sequential recovery processes. Shape memory tests revealed that the weight ratio of PLGA in the polymer composition influenced the shape fixity and shape recovery of programmed structures at body temperature. Subsequently, the developed SMPs were utilized for 4D direct ink writing printing of smart bone scaffolds. The SMPs exhibited excellent printability, enabling successful printing at 220 °C and 200 kPa, resulting in 3D-printed scaffolds with uniform and interconnected pore distribution, ensuring structural integrity. Furthermore, the 4D-printed scaffolds demonstrated outstanding degradability, biocompatibility, and mechanical properties comparable to human trabecular bone. This work presents a robust and feasible approach for 4D printing of triple-shape memory bone scaffolds, offering a promising solution for complex irregular bone defects.

1. Introduction

In recent years, extrusion-based 3D printing techniques have shown promise in biomedical applications, particularly for fabricating bone scaffolds. By depositing biomaterials layer by layer, these techniques enable the creation of complex and customized scaffolds with improved structural integrity and biological functionality. However, efficient bone defect repair remains a challenge in clinical settings. Traditional 3D printing methods produce static constructs that cannot adapt to irregular bone defect boundaries. To address this, the emerging field of 4D printing offers a solution. By introducing the dimension of time, 4D printing allows scaffolds to undergo shape and functional transformations in response to stimuli like temperature [1]. This innovative approach combines 3D printing with shape memory polymers (SMPs), creating smart scaffolds that dynamically adapt to complex defect shapes. Thermo-responsive shape memory scaffolds have the remarkable capability to deform from their primary shape to a temporarily stable shape, which can then be recovered upon exposure to heat. This unique feature allows the scaffolds to closely match the irregular contours of the target defect anatomy, promoting better integration with the surrounding tissue.

Among the various types of SMPs utilized in 4D printing, biocompatible polyesters like polycaprolactone (PCL), poly (lactic acid) (PLA), polyurethane

(PU), poly (ethylene glycol) (PEG), poly (D,L-lactic acid-co-ethylene glycol-co-D,L-lactic acid) (PELA) and their blends have demonstrated a high potential for biomedical applications including the fabrication of scaffolds in bone tissue engineering [2–9]. However, most of the previously developed SMPs for extrusion-based 4D printing of bone scaffolds are dual-SMPs, which can only memorize one temporary shape. Miao *et al* [10] utilized castor oil coupled with PCL triol to create shape memory scaffolds through indirect FDM printing. These scaffolds achieved a temporary shape at −18 °C and demonstrated a remarkable shape recovery rate of 92% upon exposure to body temperature. Similarly, Hendrikson *et al* [11] employed dual-shape memory PU in their 4D printing of scaffolds. After programming, cell seeding onto the scaffolds in their temporary shape resulted in mechanical stimulation that led to the directional growth of cells and nuclei within the 4D-printed SMP cell scaffold. Their finding highlighted the positive impact of mechanical strains on cells during the shape transformation of shape memory scaffolds. Wang *et al* [12] utilized the direct ink writing (DIW) platform to fabricate biodegradable PU–PEO scaffolds for bone tissue engineering, which exhibited dual shape memory properties at 37 °C water. Senatov *et al* [13–15] investigated shape memory PLA and PLA/15 wt.% hydroxyapatite (HA) composite bone scaffolds fabricated by FDM. The PLA/15%HA scaffold demonstrated an impressive shape recovery rate of 98%. Additionally, PELA and PELA/HA filaments were synthesized for FDM printing of porous scaffolds, exhibiting a shape recovery rate of over 90% with only one transition temperature of $T_{\text{Trans}} =$ 50 °C [16]. Furthermore, Fe_3O_4/MBG/PCL composite scaffolds with excellent magnetic heating ability and significantly stimulated proliferation were successfully fabricated using the DIW method [17].

However, multi-SMPs are particularly attractive because they can memorize and recover through more than one temporary shape, enabling a more sophisticated and controllable deployment process compared to conventional dual-shape memory systems. In the case of triple-SMPs, two temporary shapes can be sequentially programmed and recovered through distinct thermal transitions. This capability is especially relevant for bone tissue engineering, where scaffolds often need to be delivered through minimally invasive procedures and subsequently adapt to complex defect geometries. The first recovery stage can be designed to occur at or near physiological temperature, allowing the scaffold to partially expand after implantation and establish intimate contact with the surrounding defect boundaries. Such a recovery process may facilitate improved defect filling, enhanced fixation, and reduced surgical manipulation compared with conventional static scaffolds [18]. In addition to improving scaffold deployment, the second recovery stage introduces an additional level of shape programmability that may be exploited to provide controlled mechanical stimulation to cells. Previous studies have demonstrated that shape recovery in 4D-printed shape memory scaffolds can influence cell morphology, alignment, and cellular behavior by generating dynamic mechanical cues during scaffold transformation [11]. Therefore, the sequential recovery behavior of triple-shape memory scaffolds may offer unique opportunities not only for minimally invasive implantation and defect adaptation, but also for the development of dynamic cell-instructive scaffolds capable of delivering staged mechanical cues during tissue regeneration. These unique characteristics position triple-shape memory scaffolds as a promising class of smart biomaterials for next-generation bone tissue engineering applications.

One way to achieve thermally induced triple-shape memory is to fabricate physically crosslinked thermoplastic polymer blends that combine semi-crystalline and amorphous polymers with distinct crystallization and glass transition temperatures. The presence of crystalline and glassy domains within this polymer system serves as physical cross-links, which contribute to the triple shape memory effect (SME). Additionally, the effect is influenced by the composition-dependent glass transition temperature (T_g) and polymer entanglement [2, 19].

The primary objective of this research study is to integrate DIW 4D printing technology4 with innovative triple-SMPs, enabling the fabrication of thermoresponsive smart scaffolds capable of undergoing deformation and adopting two distinct shapes. To achieve this, a combination of biocompatible polymers, namely PCL, thermoplastic polyurethane (TPU), and PLGA, with separate crystallization and glass transition temperatures, is utilized. The PCL and TPU blend, recognized for its exceptional fixity and recovery performance in shape memory applications, is selected in a 50:50 ratio due to its low transition temperature [20–23]. On the other hand, the amorphous polymer PLGA, known for its high biodegradability and tunable glass transition temperature matching the body temperature, is incorporated to achieve the SME through polymer entanglements as physical cross-link points [24]. To realize the desired triple-shape memory behavior, PLGA is incorporated as the minor phase in three different weight ratios within the PCL/TPU blend. The physiochemical properties, morphology, shape memory performance, and printability of the developed SMPs are extensively evaluated, considering the impact of the DIW printing technique on material printability. Subsequently, the smart polymers are utilized for DIW printing of porous

scaffolds, which are comprehensively evaluated for morphology, structural integrity, mechanical properties, hydrolytic degradation, and cell cytocompatibility. This comprehensive evaluation aims to provide a thorough understanding of the performance and suitability of the 4D printed triple shape memory scaffolds for future bone tissue engineering applications.

2. Experimental procedures

2.1. Chemicals and raw materials

PCL with a density of 1.14 g cm^{-3} and poly (lactic-co-glycolic acid), 50:50 (PLGA 50:50) with a density of 1.53 g cm^{-3} were provided by BOC Science Co. Adipic acid-based TPU with a density of 1.21 g cm^{-3} purchased from redox plastics (Ellastolan). Dulbecco's modified eagle's medium (DMEM), fetal bovine serum (FBS), L-glutamine, 0.5% trypsin-EDTA, and penicillin-streptomycin (pen-strep) were purchased from Invitrogen/Gibco Co. A CellTiter 96® AQueous One Solution cell proliferation assay kit was purchased from Promega Co.

2.2. Material and sample preparation

Using a twin-screw mixture (model: HAAKE Polylab QC), (50 wt.% TPU/50 wt.% PCL)/PLGA blends with different weight ratios of PLGA 10, 20 and 30 wt.% were prepared. The mixing screw speed, temperature and period were set at 100 rad min^{-1}, 150 °C, and 10 min, respectively. Blended materials were first cut into granules and then used for characterization and direct write printing. The sample labels and corresponding compositions for all polymer blends are summarized in table 1, where C represents pure PCL, U pure TPU, and G pure PLGA.

2.3. Printability assessment

To assess the printability of the developed UC and UCG SMPs, a series of printability experiments were conducted using a pneumatic extrusion-based 3D bioprinter (BIO X CELLINK, Sweden). The printer was equipped with a thermoplastic printhead capable of withstanding temperatures up to 250 °C. Firstly, UCG granules were transferred into a stainless-steel cartridge, which was then inserted into the thermoplastic printhead. The printhead, along with the cartridge, was attached to the BIO X print box for further processing. To evaluate the printability, a cubic 3D CAD model measuring 20 × 20 × 1 mm^3 (length × width × height) was designed using SolidWorks software. The CAD files were then imported into the BIO X printer, where the Heart OSTM software was used to slice the model. The model was sliced into a grid-like 4-layer scaffold with a 40% infill density. During the printing process, all parameters were kept at their default settings in the Heart OSTM software, except for the extrusion temperature, which varied between 200 °C and 240 °C, and the pressure, which ranged from 190 to 300 kPa. These variations allowed for the evaluation of different printing conditions and their impact on the printability of the UC and UCG SMPs.

Table 1. Sample names and corresponding compositions for all UCG blends.

Sample names	PLGA content (wt.%)	PCL content (wt.%)	TPU content (wt.%)
UC	0	50	50
10% G	10	45	45
20% G	20	40	40
30% G	30	35	35

Table 2. Optimized DIW printing parameters for UCG SMPs.

Parameter	Value
Nozzle diameter, mm	0.41
Pressure, kPa	200
Nozzle temperature, °C	220
Print bed temperature, °C	25
Layer height, mm	0.2
Print speed, mm s^{-1}	10
Infill percentage, %	40
Pre- and post-flow time, ms	0

2.4. Scaffold design and fabrication

For the scaffold fabrication, a cylindrical structure with a diameter of 10 mm and a height of 5 mm was designed using SolidWorks software. The CAD model was then sliced using the Heart OSTM software, resulting in a rectilinear lay-down pattern with a 40% infill density, equivalent to 60% porosity [25]. Scaffolds were then printed using the parameters listed in table 2.

2.5. Cytotoxicity analysis by MTS assay

Human osteoblast-like MG-63 cells were purchased from ThermoFisher Scientific. Cell proliferation was evaluated using an MTS assay after culturing for 1 d, 3 d, and 7 d using the CellTiter 96 AQueous One Solution kit (Promega Life Sciences). First, UC and UCG scaffolds were cut into disk-shaped samples (5 mm diameter and 1 mm height). The scaffolds were then sterilized by immersing them in 75% ethanol for 30 min. After this, each side of the scaffold was exposed to UV light for 1 h. To improve cell attachment, the scaffolds were then incubated overnight in DMEM solution containing 10% FBS, 2 mM L-glutamine, and 100 U ml^{-1} penicillin-100 μg ml^{-1} streptomycin. Following this, the growth media was removed, and the scaffolds were transferred to a new

96-well plate, and MG-63 cells were cultured at a density of 5000 cells per well. Upon testing, cells were treated with media containing 20% MTS solution and allowed to incubate for 1 h. Then, 100 μl of spent media were transferred into a clear 96-well plate. The absorbance of the plates at a wavelength of 490 nm was read and recorded using a microplate reader. The statistical data is presented as mean ± standard deviation. The data were analyzed using the two-way analysis of variance method. Tukey's multiple tests were then used to evaluate the specific differences of the data, and these differences were considered statistically significant at different levels: ns = not significant, $^{*}p < 0.05$, $^{**}p < 0.01$, $^{***}p < 0.001$, $^{****}p < 0.0001$.

2.6. Characterization techniques

2.6.1. X-ray diffraction (XRD) analysis

Rectangular-shaped specimens with a size of 10 mm × 10 mm × 4 mm were printed for the XRD test, and the crystalline and amorphous phase of developed SMPs were characterized by using a Cu source x-ray diffractometer (Aeris Research/Malvern Analytical, United Kingdom). The XRD experiments were carried out at an accelerating voltage of 5 kV and an emission current of 1000 mA with step size 0.01 (2θ) from 10° to 80°.

2.6.2. Differential scanning calorimetry (DSC)

The thermal properties of the developed polymers were investigated using DSC (NETZSCH DSC 204F1 Phoenix) under a nitrogen atmosphere. Samples weighing 15 mg each were encapsulated in an aluminum pan with a lid, and the following heating and cooling cycles were applied to each sample: The samples were first kept at −70 °C for 5 min, then heated up to 150 °C at a heating rate of 10 °C min^{-1}. After this, to allow the samples to equilibrate, they were kept at 150 °C for 5 min. Then the samples were cooled down to −70 °C at a cooling rate of 10 °C min^{-1}. Following this, the samples were stabilized at −70 °C for 5 min, and then the second heating cycle ran up to 150 °C and at the same heating rate of 10 °C min^{-1}. In the end, the sample was kept at 150 °C for 5 min.

2.6.3. DMA

To study the thermal dynamic properties of UCG materials, we conducted tests in single cantilever mode using a TA Q800 instrument (New Castle, DE) in 'multi-frequency strain' mode. Rectangular test samples measuring 40 × 8 × 1 mm^3 were prepared and tested over a temperature range of 25 °C–100 °C, with a heating rate of 3 °C min^{-1} and a frequency of 1 Hz. To maintain a consistent temperature during heating and cooling, liquid nitrogen was used.

2.6.4. Morphology

Scanning electron microscopy (The Hitachi 3400I SEM, Japan) was used to evaluate the microstructure and morphology of developed UCG polymers and DIW-printed scaffolds. SEM imaging technique was also used to examine the morphology of adhered cells on the UCG scaffolds. The freeze-fractured surfaces of all samples were prepared by submerging them in liquid nitrogen (LN_2), followed by breaking them manually prior to SEM imaging. Prior to SEM imaging and by using a sputter coater (Quorum, Q300 model), all samples were platinum coated with a terminate thickness of 15 nm and 30 mA sputter current.

2.6.5. Shape memory test

To assess the SME of the developed materials, a U-bending test was conducted. Samples measuring 50 mm in length, 8 mm in width, and 1 mm in thickness were prepared. The test was carried out in six steps as follows: (1) the samples were heated to 70 °C and bent from approximately 180° to 90° ($\theta_{\mathrm{Load|A}}$) and held at 45 °C for two minutes; (2) the sample was kept at 40 °C without any external force for five minutes ($\theta_{u|\mathrm{A}}$); (3) the sample was bent from 90° to 135° ($\theta_{\mathrm{Load|B}}$) at 45 °C and then cooled to room temperature for two minutes; (4) the sample was kept at room temperature free of force for five minutes ($\theta_{u|\mathrm{B}}$); (5) the sample was heated to 37 °C for the first recovery ($\theta_{p|\mathrm{B}}$); (6) the sample was then heated to 70 °C for the second recovery ($\theta_{p|\mathrm{A}}$). Photographs were taken at the end of each step, and the actual angles were measured. The shape fixity (R_{f}) and recovery (R_{r}) ratios were defined as follows [26, 27]:

$$R_{\mathrm{f}}(X \to Y) = \left(\theta_{u|Y} - \theta_{u|X}\right) / \left(\theta_{\mathrm{Load}|Y} - \theta_{u|X}\right) \times 100 \quad (1)$$

$$R_{\mathrm{r}}(Y \to X) = \left(\theta_{\mathrm{Load}|Y} - \theta_{p|Y}\right) / \left(\theta_{\mathrm{Load}|Y} - \theta_{u|X}\right) \times 100 \quad (2)$$

X and Y represent different states of samples (two temporary shapes and a permanent shape).

2.6.6. Mechanical properties of UCG scaffold

The mechanical properties of the 3D printed scaffolds were evaluated by compression test using a universal testing system (Instron testing machine 3369 model) equipped with a 10 kN load cell. In accordance with ASTM D695-15 standard, printed scaffolds ($n = 3$ per group) were compressed based on an 80% deformation at a constant crosshead speed of 1 mm min^{-1} at room temperature. Scaffold surface area was measured prior to the mechanical assessment and the slope of the straight-line portion of the stress–strain curve was used to calculate the compressive modulus.

2.6.7. Hydrolytic degradation

To evaluate the hydrolytic degradation of UCG scaffolds, disk-shaped samples with a diameter of 5 mm and height of 2 mm were prepared and immersed in phosphate-buffered saline (PBS) at 37 °C for 120 d. The PBS solution was exchanged every two days to ensure consistent conditions, and at regular weekly intervals, the samples were removed, washed with deionized distilled water, and dried in a vacuum oven at 45 °C for 48 h. The weight loss of the scaffolds was then recorded, and the percentage of remaining weight was calculated using the formula (5–3):

$$\text{Remaining weight} = W_f/W_i \times 100 \quad (3)$$

where W_f represents the weight of the scaffold at the time of removal, and W_i represents the initial weight before soaking on day 0.

2.6.8. Surface wettability

The surface wettability of all scaffolds was measured by distilled water using theta optical tensiometer (Attension, Biolin Scientific, Finland) equipped with an auto dispenser and a video camera. A sessile DI water droplet was placed on the cross section of the UCG scaffolds, and images of the droplet spreading over 60 s were recorded. For each drop, an average of 30 frames were analyzed, and the contact angles were calculated.

3. Results and discussions

3.1. Preparation and characterization of triple shape memory UCG

Among all kinds of thermo-responsive SMPs, the physically crosslinked thermoplastic polymer blends composed of semi-crystalline and amorphous polymers with separated crystallization and glass transition is an important material system exhibiting triple shape memory properties [27, 28]. TPU/PCL binary blend was chosen as the main matrix, In the TPU/PCL blend system, PCL crystalline domains act as reversible switching segments controlling the shape memory response, while the TPU phase provides physical net points that preserve the permanent structure and supply the elastic restoring force. Below the melting temperature (T_m) of PCL (~58 °C), PCL crystallization restricts polymer chain mobility and stabilizes the programmed temporary shape, contributing to high shape fixity. Upon heating above T_m, melting of the PCL crystalline domains increases molecular mobility, allowing the stored elastic energy within the network to drive shape recovery [28, 29]. The melting temperature of PCL is denoted as T_{high}. PLGA with a 50:50 ratio of lactic acid to glycolic acid, was chosen as another component. PLGA 50:50 is a biodegradable and biocompatible amorphous polymer with a relatively low glass transition (T_g) temperature close to body temperature, denoted as T_{low}, the entanglements of polymer chains at its glass transition temperature act as physical cross-link points, determining its permanent shape and enabling SMEs [24, 30, 31]. The predicted structure of the UCG polymer material is illustrated in figure 1(a). In this structure, the skeleton of the UC polymer is fabricated by the crosslinked and crystallizable PCL and the amorphous PLGA fills the interspace of the UC skeleton. The UCG polymer system can be programmed to achieve two distinct shapes, referred to as shape A and shape B (figure 1(b)). Shape A is achieved by heating the sample above T_{high}, which softens the PCL segment and makes it flexible, and applying a force to reshape it. Then, while maintaining the force, the sample is cooled above T_{low} to securely fix it into shape A. On the other hand, shape B is achieved when the PLGA component softens to a rubbery state within the temperature range of $T_{low} < T < T_{high}$. During cooling to $T < T_{low}$, the reordered polymer chains in shape B are fixed, preserving the second shape. Shape B and shape A recovery of the UCG polymer are achieved by reheating it to temperatures higher than the programming temperatures. It is worth noting that the SME of the developed triple polymer system is tunable by varying the ratio between PLGA and UC segment.

The thermal properties of UCG blends evaluated by DSC, the XRD profiles, the dynamical mechanical properties evaluated by DMA, and the morphology of UCG blends evaluated by SEM are shown in figure 2. The heating curves (figure 2(a)) showed an endothermic peak corresponding to the melting temperature of the crystalline phase, identified as PCL in the UCG samples. The melting temperatures of 10% G and 20% G samples were found to be 57 °C, while the 30% G sample exhibited a slightly lower melting temperature of 56 °C. The samples also showed an apparent glass transition temperature of around 34 °C, which was attributed to the T_g of PLGA polymer. Neat PLGA displayed a glass transition temperature of 41 °C. Hence, the addition of PLGA to the UC blend resulted in a decrease in the glass transition temperature of UCG samples compared to neat PLGA. As previously mentioned, PLGA is an amorphous polymer that exhibits SME due to physical cross-linking points formed by polymer entanglements. These cross-linking points allow PLGA to retain a permanent shape. The T_g serves as the transition temperature for the SME in PLGA blended polymers. Above the T_g, increased molecular mobility enables the polymer chains to rearrange and retain a permanent shape [24]. Therefore, it is expected that the developed UCG blends will exhibit SME when heated up to their T_g which is 34 °C. It was also observed that the UC polymer exhibited a cold crystallization temperature (T_c) of 32 °C, which increased to 33 °C upon adding PLGA to the UC polymer (figure 2(b)). These results suggest that adding PLGA may inhibit the crystallization of PCL in the

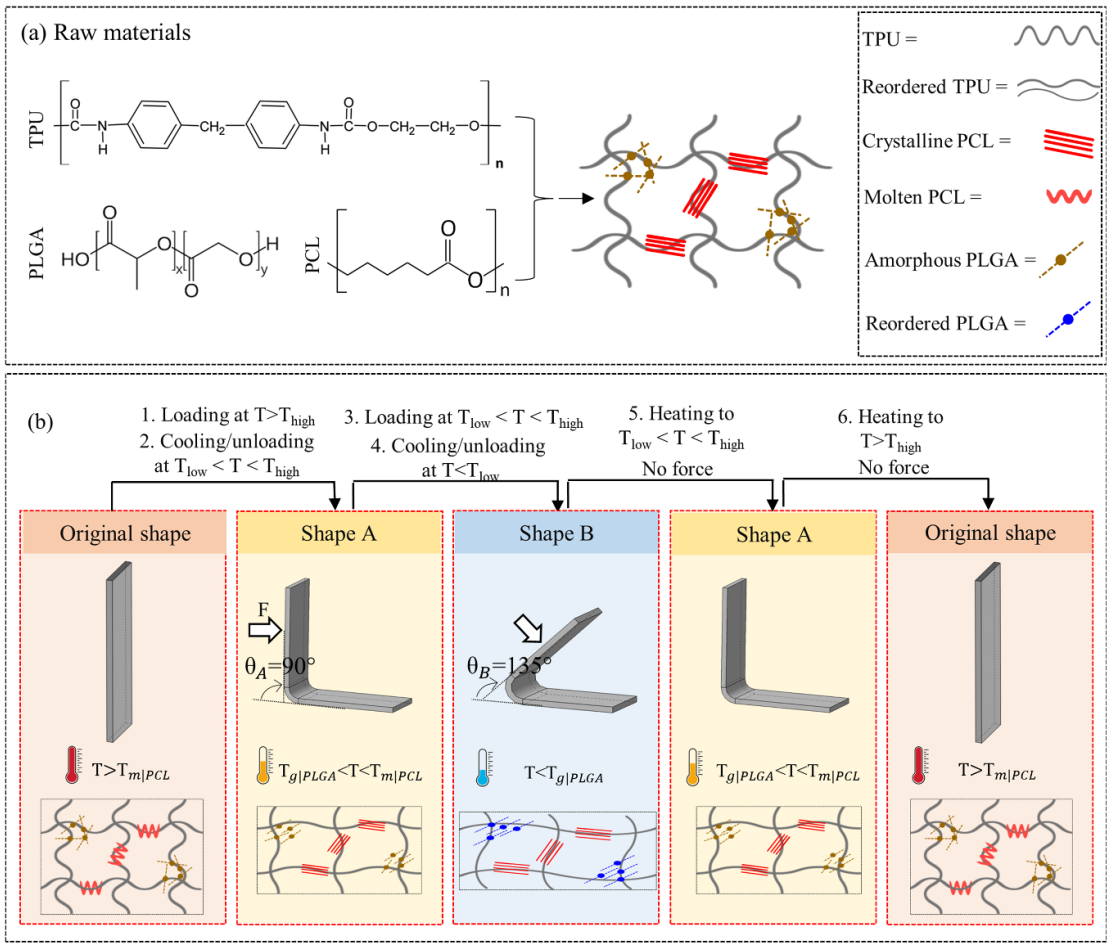

Figure 1. (a) Raw materials and molecular segments of the developed triple SMP, (b) schematic illustration of the experimental process for programming and shape recovery in SMP bars, involving molecular semi-crystalline transformations. Shape memory programming is accomplished by initially heating the sample to 70 °C ($T > T_{high}$), resulting in the melting of the PCL component and material softening with increased polymer chain mobility. Simultaneously, while maintaining the sample temperature at 70 °C, an external load is applied to deform the material. With the applied force maintained, the sample is cooled to 45 °C ($T_{low} < T < T_{high}$). Shape B is achieved by further deforming the sample at this temperature, which causes the reordering of the PLGA segment, and is fixed upon cooling to 25 °C ($T < T_{low}$). Shape B and shape A recovery of the UCG polymer are achieved by sequentially reheating the sample to temperatures higher than the programming temperatures.

UCG polymers, potentially affecting their shape A-fixing properties.

The changes in the storage modulus were examined using DMA at a fixed frequency of 1 Hz against temperature. As shown in figure 2(c), the two drops observed for all UCG samples in positions of T (25 °C–40°C) $< T_{g|PLGA}$ and $T_{g|PLGA} < T$ (55 °C–70°C) $< T_{m|PCL}$. The first drop in the storage modulus occurred sharply around 40 °C due to the glass transition phase associated with the presence of PLGA polymer in the blend, and the steepness of this drop became more pronounced with an increase in PLGA content. The second drop in the storage modulus, which occurred around 60 °C, is associated with melting in the crystalline PCL regions of the UCG polymers. Furthermore, it was observed that the storage modulus of all materials increased over the range of 25 °C–40°C temperature region by incorporating PLGA into the polymer blend network. This suggests that the presence of increased PLGA in the polymer blend network could create larger shape B recovery stress by enhancing the storage modulus [32]. Furthermore, as the storage modulus decreases in two stages, the deformed strain can be expected to be released in two steps, further confirming the sequential recovery of developed UCG polymers.

The XRD analysis of the UCG polymers revealed their semi-crystalline nature, confirming the presence of both crystalline and amorphous domains in the developed triple SMPs (figure 2(d)). The analysis showed two sharp crystallization peaks at 21° and 24°, corresponding to the (110) and (200) lattice planes of the PCL polymer. However, upon adding PLGA content, the intensities of the crystalline peaks related to the (110) and (200) lattice planes decreased and broadened compared to UC composition. The broadening of the peaks and decreased intensities progressively increased with higher PLGA content. The XRD data suggests that the diffraction pattern results of the UCG blend corresponded to the sum of the patterns for TPU, PCL, and PLGA, indicating the presence of both crystalline and amorphous

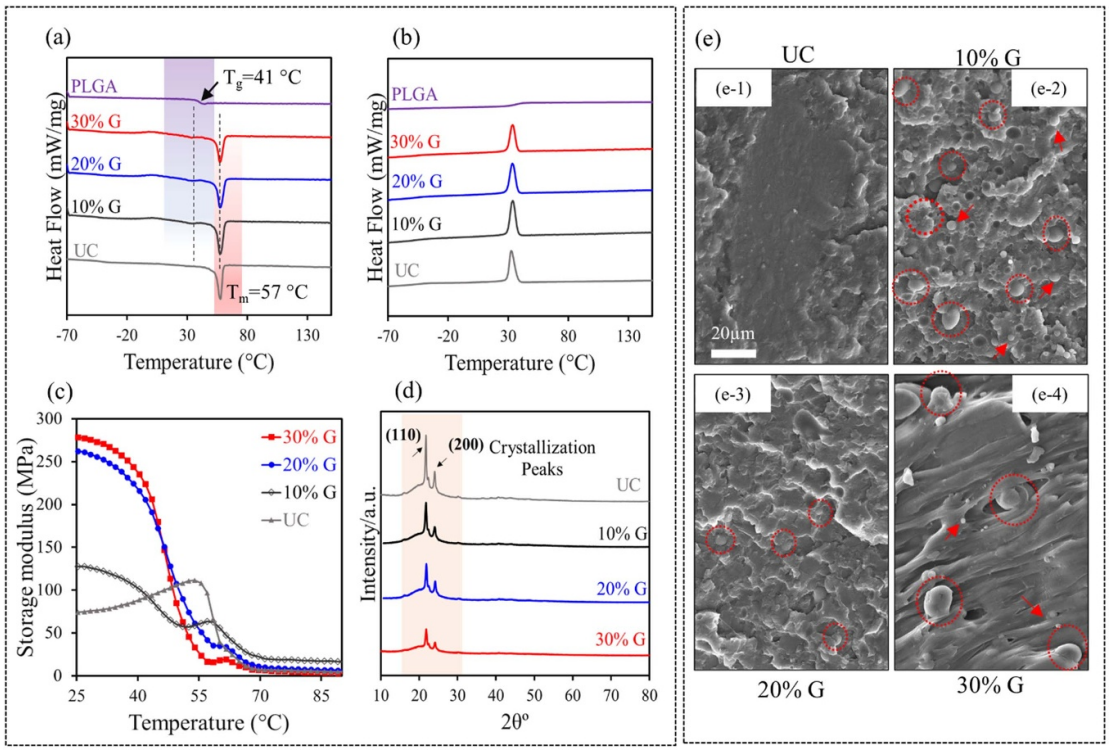

Figure 2. (a), (b) DSC thermographs showing the heating and cooling curves of UC and UCG SMPs, confirming the presence of distinct melting and glass transition temperatures in the developed UCG blends, (c) storage modulus of the blends as a function of temperature, (d) XRD diffraction pattern of UC and UCG SMPs, (e) SEM images of the cryo-fractured surfaces of the developed materials, including (e-1) UC, (e-2) 10% G, (e-3) 20% G, and (e-4) 30% G blends.

phases in the blend. Furthermore, these findings suggest that the incorporation of PLGA can influence the crystalline structure of the UCG polymers, potentially impacting the fixity and recovery performance of both shape A and shape B.

To better understand the phase behavior and miscibility of the developed blends, we analyzed the morphology of the cryo-fractured surfaces of all polymer blends using the SEM technique. As figure 2(e)-1 shows, the UC binary blend exhibited a smooth fracture surface with no obvious phase boundaries, indicating that PCL and TPU at a weight ratio of 50:50 wt.% can form a miscible and homogeneous blend. Conversely, the droplet-matrix morphology was detected for all UCG blends, where the spherical droplets of PLGA were dispersed in the matrix of the UC phase and the boundary between the phases was easily recognized [33]. The size and distribution of the dispersed PLGA phases varied with the PLGA concentration. In the 10% G and 20% G samples, small PLGA phases were uniformly distributed, with more spherical droplets observed in the 10% G sample. The size of the dispersed phase increased for the 30% G sample (figure 2(e-4)). These results are consistent with the behavior of immiscible polymer blends, where the minor component is dispersed in the matrix of the major component [34]. All SEM micrographs of UCG polymer blends demonstrated that UC and PLGA are immiscible. However, for the 20% G blend, a lower number of dispersed PLGA particles can be observed, suggesting improved blending performance and potentially resulting in better mechanical performance.

The results obtained from the shape memory tests are presented in figure 3 and table 3. Shape fixing (R_f) and shape recovery (R_r) ratios were calculated using equations (1) and (2), and the data were plotted in figure 3(c) for UC and UCG blends. It was observed that increasing the PLGA content resulted in a higher shape B fixity ratio, while the shape B recovery ratio at body temperature (37 °C) gradually decreased. This behavior can be attributed to the dual role of PLGA in the TPU/PCL/PLGA blend system. As the PLGA content increased, additional PLGA-rich domains and polymer chain entanglements were formed, restricting molecular mobility below the glass transition temperature (T_g) and improving the stability of the programmed temporary shape B. Consequently, the shape B fixity ratio increased with increasing PLGA content. However, the higher rigidity of PLGA and the increased phase separation at elevated PLGA concentrations also restricted the mobility of the recoverable polymer network. This reduced the ability of the material to release the stored elastic strain energy required for shape recovery at body temperature, leading to a decrease in the shape B recovery ratio. Therefore, while higher PLGA contents enhanced temporary shape stabilization, they simultaneously

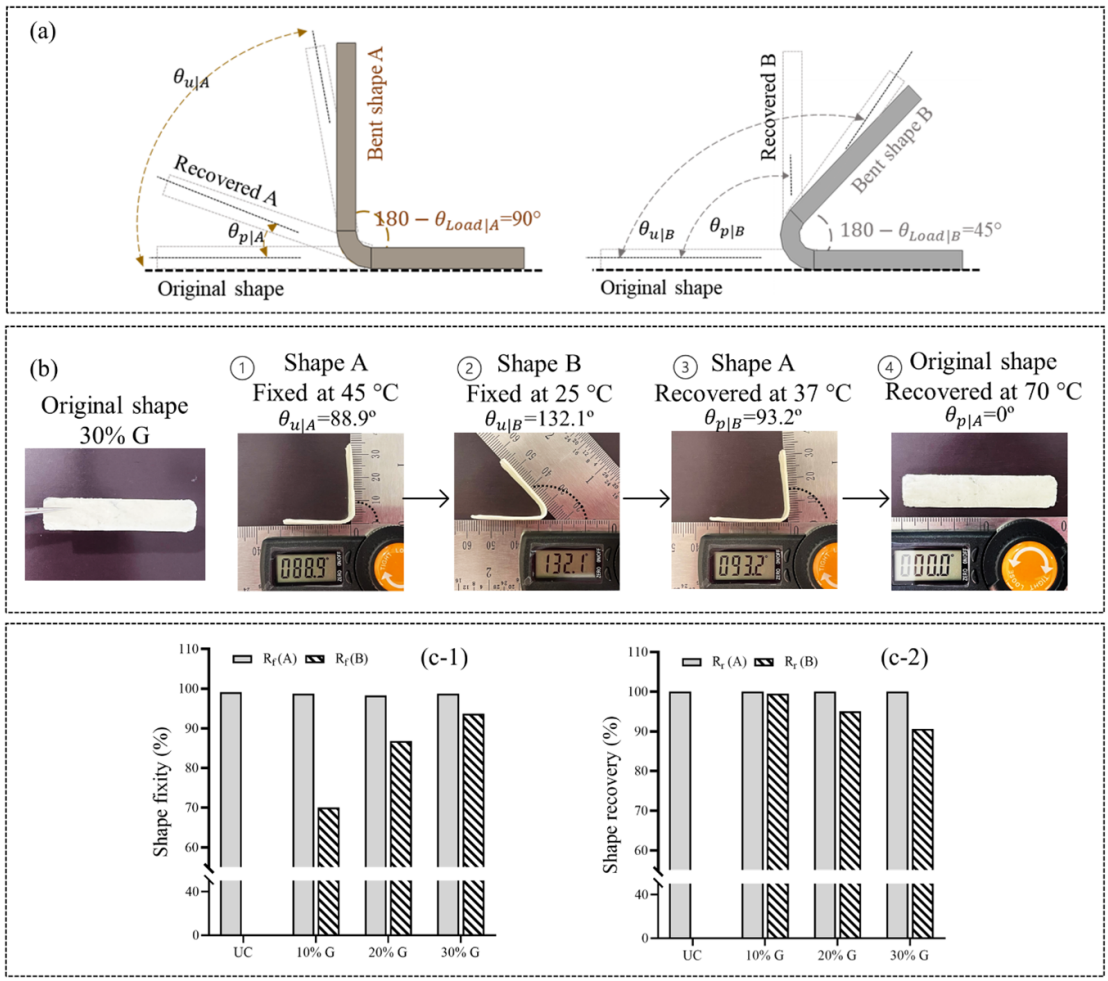

Figure 3. (a) Schematic illustration of bending test for shape memory effect, (b) illustration of photographs of triple shape memory effect in 30% G sample, (c-1, c-2) shape fixity and shape recovery ratios of UC and UCG samples obtained according to formulas (1) and (2).

Table 3. Triple-shape-memory effect data of UCG SMPs according to formulas (1) and (2).

Sample	$\theta_{u\|A}$	$\theta_{u\|B}$	$\theta_{p\|B}$	$\theta_{p\|A}$	R_f (A)	R_f (B)	R_r (B)	R_r (A)
UC	89.1°	—	—	0°	99.1%	—	—	100%
10% G	88.9°	121.2°	89.1°	0°	98.7%	70%	99.5%	100%
20% G	85.5°	128.8°	90.8°	0°	98.3%	86.8%	95.05%	100%
30% G	88.9°	132.1°	93.2°	0°	98.7%	93.7%	90.6%	100%

limited the recovery efficiency of the scaffold. The presence of distinct crystalline and amorphous phases within the blends, as confirmed by DSC, DMA, and XRD analyses, supports this shape memory mechanism. All UCG blends demonstrated shape recoveries of over 90%, indicating a good shape recovery ability [35]. Furthermore, all UC and UCG exhibited shape A fixity ratios exceeding 98% and achieved complete shape B recovery when subjected to a temperature of 70 °C. This exceptional behavior can be attributed to the fact that the shape memory behavior of the material is affected by temperature, with recovery values differing between the programming temperature (70 °C) and the transition temperature (∼57 °C). The transition temperature is the temperature at which the material undergoes a phase change that allows it to recover its original shape. When the material is heated above this temperature, it undergoes a phase transition and the stored strain is released, allowing it to fully return to its original shape.it is important to note that the shape recovery process is not fully completed at the transition temperature, as the material requires additional heating above the transition temperature for complete stress relaxation and to fully recover its original shape [36].

While the present study successfully demonstrates a body-temperature-responsive triple-SME with high shape fixity and recovery ratios, future work should investigate cyclic shape memory performance under repeated programming and recovery cycles to assess

long-term durability and repeatability for biomedical applications.

Figure 3(b) includes photographs depicting the U-bending test conducted on the 30% G sample, showcasing the fixing angles and recovery at shape A and shape B.

3.2. Printability assessment

In the DIW process of thermoplastic polymers, the extrusion efficiency and quality of the 3D printed structure are significantly influenced by the viscosity and the amount of material extruded from the nozzle. Therefore, careful design of printing parameters, particularly nozzle temperature and print pressure, is crucial to ensure consistent material flow and precise layer deposition [37]. Print pressure plays a critical role in controlling the flow rate of the extruded ink. When the pressure is too high, it can cause the material to spread out too much or even break apart, leading to a loss of structural integrity and a decrease in fidelity. Additionally, high pressure can result in clogging of the bioprinting nozzle. This issue can cause disruptions in the printing process and adversely affect the fidelity of the scaffold [38]. On the other hand, low print pressure may cause under-extrusion, where the extruded ink fails to adhere properly, resulting in weak interlayer bonding and reduced structural integrity. Similarly, print temperature is another important parameter that needs to be carefully controlled [39]. The appropriate print temperature ensures good flow properties of the ink, allowing for a controlled and uniform filament width. If the print temperature is set too high, the deposited filament can become swollen and lose its shape fidelity. Conversely, if the print temperature is too low, the ink may not flow properly, leading to insufficient material deposition and poor layer adhesion. Therefore, it is essential to optimize the print pressure and temperature parameters. This ensures that the flow is high enough to extrude the ink. However, it should not be so high that it compromises the fidelity of the resulting scaffold. This optimization is crucial for achieving the desired print quality and structural integrity. In this study, we evaluated the printability of newly developed materials by designing and printing a 2-layer CAD model scaffold with 40% infill. We conducted this assessment by printing the CAD design using various temperatures and pressures to optimize each ink formulation. Initially, we determine the starting point for print temperature and pressure based on the manual filament dispensing test [38, 40]. This method involves extruding a filament into the air rather than on a substrate and serves as an initial screening technique, focusing on the ink's ability to form filaments rather than droplets. The printing pressure and temperature that successfully yield filaments passed the initial printability assessment. Then we developed a printability window for each material formulation by evaluating the filament characterization and shape fidelity of the printed constructs. This assessment was conducted at temperatures ranging from 200 °C to 240 °C and pressures ranging from 190 to 300 kPa (figure 4(b)). These parameters determine the level of dimensional accuracy achieved compared to the original design [37, 41]. The results, including the printability window, optical images of printed construct and quantitative tests for assessing shape fidelity, are summarized in figure 4. In figure 4(b), white printing windows with green tick marks indicate the successful printing of well-defined structures at various printing pressures and temperatures. The yellow exclamation mark in the printability window indicates the printing temperature and pressure at which the structure is partially printable. At this point, the filament forms with available pores, but the resulting shape and size are not as desired as seen in figure 4(c-8). Grey and pink colors represent pressure and temperature values that were too low or too high, respectively. It was observed that at the pressure of 200 and 225 kPa all developed materials were able to form consistent filaments with acceptable structural stability and cohesion, so they were deemed printable (figure 4(c)).

At a printing temperature of 220 °C and a pressure of 250 kPa, full filament merging occurred for all developed inks, resulting in pore closure. This condition is represented as pink in the printability window. We observed that the starting temperature of the printability window increased with the percentage of PLGA in the polymer composition. For instance, at a printing pressure of 200 kPa, the UC blend was printable at a temperature of 200 °C, while compositions containing 20% G and 30% G required a higher temperature of 220 °C for printability. The same trend was observed when printing at a pressure of 225 kPa.

As a result, the printability window became narrower when using inks with higher PLGA content. This can be attributed to the immiscible nature of UCG blends, as shown in figure 2(e). Immiscible blends typically exhibit poor flowability due to the presence of dispersed domains or phase boundaries. To address this, increasing the temperature moderately is often recommended. This helps reduce the viscosity of the individual polymers, allowing for easier flow and improved overall flow properties of the blend [42]. However, it should be noted that temperatures above 230 °C resulted in polymer swelling and structural failures for all developed SMPs.

Optical microscopy imaging results demonstrated the excellent structural integrity of all developed inks when printed at 220 °C temperature and 200 or 225 kPa printing pressures (figures 4(c-9) to 4(c-16)). The 3D-printed constructs displayed a uniform and interconnected pore distribution throughout their structure, without any impurities or cracks. However, there was a noticeable difference in the size of struts and pores between scaffolds printed at 200 and 225 kPa. Constructs printed at 225 kPa had

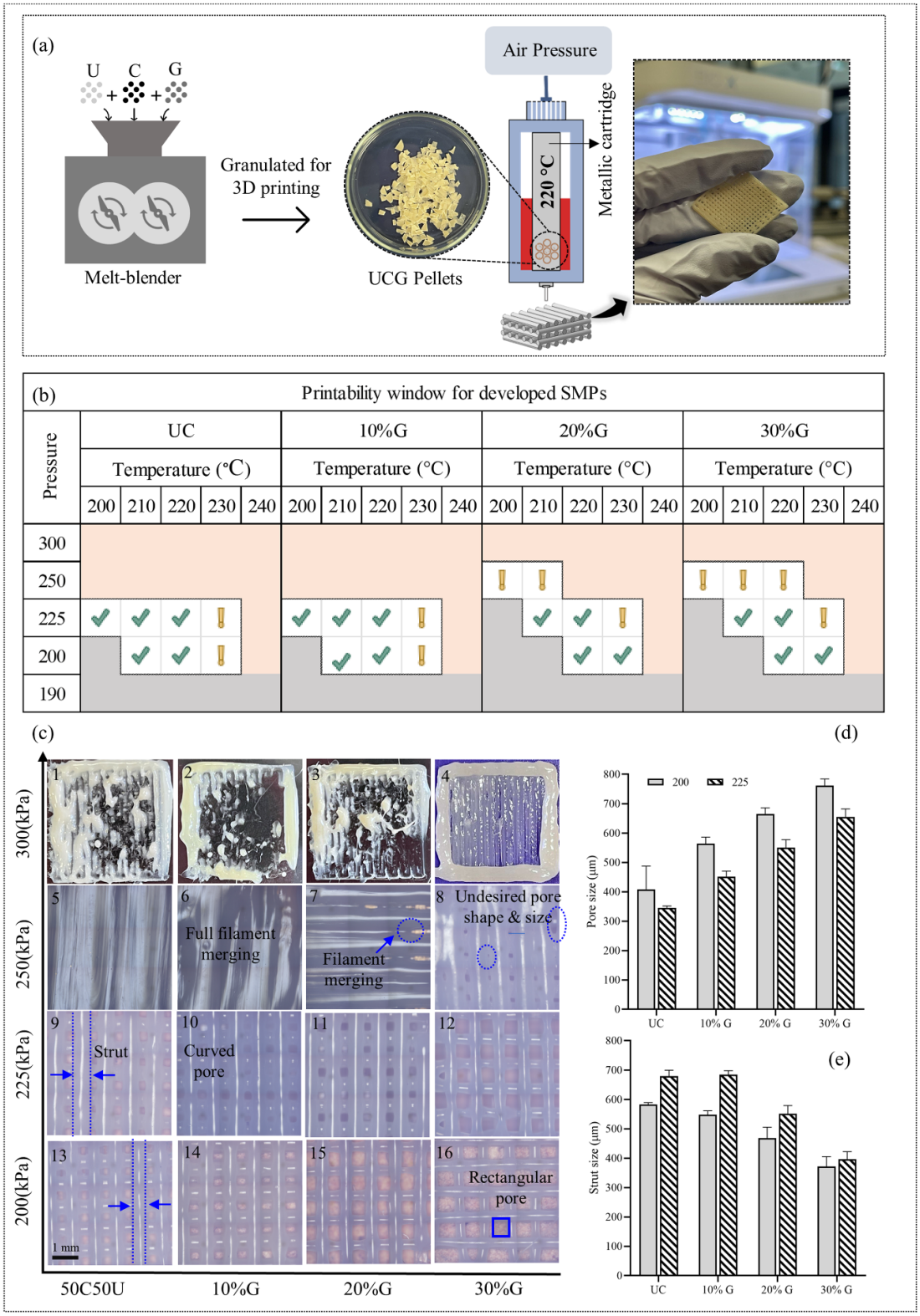

Figure 4. (a) Schematics illustrating the preparation of UCG SMPs and the fabrication of shape memory scaffolds using the DIW process, (b) printability window calculated for the four developed SMPs: UC, 10% G, 20% G and 30% G. The optimal printing pressure and temperature are indicated by green tick marks, while the yellow exclamation mark denotes a printable condition with low shape fidelity. Pink indicates printing conditions where pressure and temperature were too high, and grey indicates conditions where pressure and temperature were too low for successful printing, (c) layer stacking optical microscopy results of UC and UCG polymers printed at a temperature of 220 °C and pressures ranging from 200 kPa to 300 kPa, (d) strut (filament) width analysis of DIW-printed UC, 10% G, 20% G, and 30% G patterns, (e) pore size analysis of DIW-printed UC, 10% G, 20% G, and 30% G patterns.

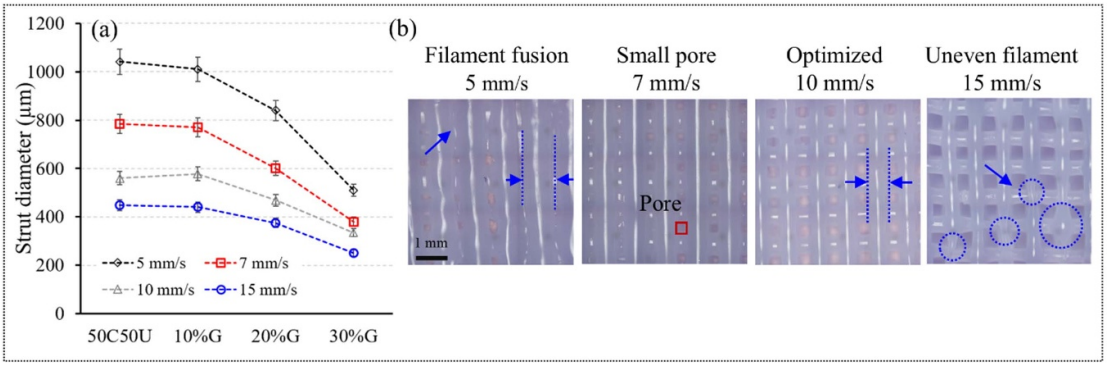

Figure 5. (a) Analysis of strut size in DIW-printed UC and UCG patterns using a temperature of 220 °C and pressure of 200 kPa at different print speeds, (b) optical microscopy results of layer stacking in UC scaffolds printed at a temperature of 220 °C and pressure of 22 kPa with varying print speeds.

wider struts and smaller pore sizes compared to those printed at 200 kPa (figure 4(e)). For example, for the 10% G ink, constructs printed at 225 kPa exhibited a strut size of 694 μm and a pore size of 460 μm, while those printed at 200 kPa had a strut size of 578 μm and a pore size of 550 μm. Furthermore, there was an inverse relationship between the strut size and the PLGA content in the polymer composition. At a printing temperature of 220 °C and a pressure of 225 kPa, the strut sizes for constructs containing 10% G, 20% G, and 30% G were measured as 694 μm, 565 μm, and 370 μm, respectively. It is crucial to ensure that the scaffold possesses a suitable pore size to support cell proliferation, differentiation, and tissue growth. It has been recommended that scaffolds with pore sizes exceeding 300 μm are most effective for repairing large bone defects [43–45]. Therefore, selecting appropriate printing parameters to achieve these desired pore sizes is important for scaffold functionality. Based on the printability assessment, it was found that printing at a temperature of 220 °C and either a pressure of 200 kPa or 220 kPa resulted in achievable pore sizes ranging between 352–718 μm. Notably, when printing at lower pressures, the pore shape appeared more rectangular, while higher pressures led to a curved shape due to the flow dynamics.

The influence of printing speed on ink deposition was also assessed for all developed SMP inks. It was observed that at a fixed printing temperature of 220 °C and pressure of 200 kPa, the width of the printed filament varied with different printing speeds, as shown in figure 5(a). It was observed that increasing the printing speed resulted in a decrease in strut width for all compositions. Figure 5(b) presents optical microscopy images of a 3D construct printed at a temperature of 220 °C and pressure of 200 kPa, using UC composition. When the print speed was set at 5 mm s^{-1} filament fusion and pore closure were observed. Increasing the speed to 7 mm s^{-1} resulted in filament stretching and reduced filament width to 784 μm, accompanied by a small pore size of 180 μm. At a speed of 10 mm s^{-1}, the filament width was 560 μm, with a pore size of 391 μm, which was selected as the optimized speed. However, further increasing the speed to 15 mm s^{-1} led to interrupted deposition, uneven filament formation, and a loss of consistent and uniform filament diameter. After considering the results, the temperature of 220 °C, printing pressure of 200 kPa, and printing speed of 10 mm s^{-1} were selected as the optimum nozzle temperature, extrusion pressure, and printing speed parameters.

3.3. Scaffold fabrication and characterization

Figure 6(a) illustrates the 3D printed scaffolds with a diameter of 10 mm and a height of 5 mm and SEM images of their top surfaces, showcasing the porous structures of UC, 10% G, 20% G, and 30% G scaffolds printed with 40% infill density. The SEM imaging results showed that all 3D printed scaffolds exhibited a uniform and interconnected pore distribution throughout their structure. Notably, all of the designed scaffolds were fabricated with excellent structural integrity, without any impurities or cracks in their structure. Furthermore, the surface characteristics of the scaffolds appeared remarkably smooth, with no apparent signs of phase separation or discontinuities. The pore sizes obtained were 391 μm, 550 μm, 674 μm, and 718 μm for scaffolds made of UC, 10% G, 20% G, and 30% G materials, respectively. As discussed earlier, the observed decrease in pore size can be attributed to the immiscibility of the UCG composition and the comparatively lower viscosity of the PCL component in the blend. For example, in the case of UC scaffolds, 50% of the composition consists of PCL. However, for scaffolds with 30% G, only 35% of the composition is made up of PCL. This difference in PCL content directly influences the flowability and viscosity of the ink during printing.

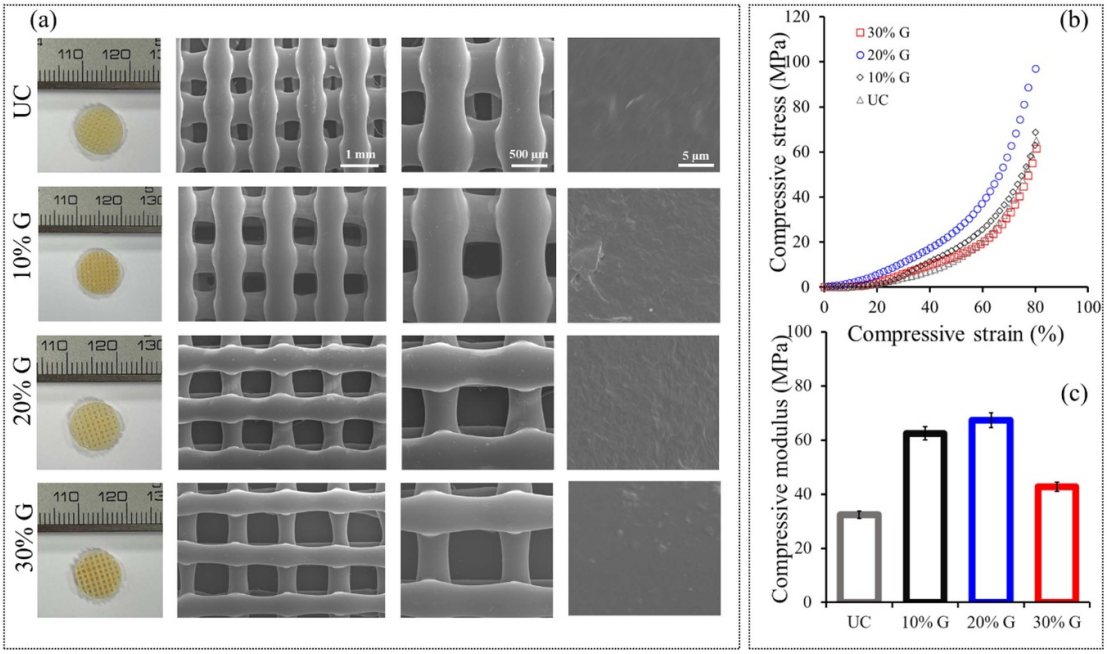

Figure 6. (a) Macroscopic surface structures of the 3D-printed scaffolds of UC and UCG SMP blends, (b) stress–strain plots, and (c) compressive modulus of all DIW-printed scaffolds.

With a higher proportion of PCL in the blend, the ink exhibits improved flow properties, resulting in a wider filament width and smaller pore sizes in the printed scaffolds.

One of the fundamental requirements for scaffolds is to possess adequate mechanical strength to withstand the stresses imposed on them during tissue growth and regeneration. The mechanical properties of scaffolds are significantly influenced by the material composition used during printing [46]. The evaluation of compression properties of our 3D printed UC and UCG scaffolds is shown in figures 6(b) and (c). All scaffolds were subjected to a total strain of 80% and the stress–strain curves for the scaffolds showed three stages. The first stage with linear behavior was related to elastic response, followed by a nonlinear increase in stress as the material approached the plateau regime. This behavior indicated a lack of failure and stretching of the struts. As compression continued, the material densified and its strength increased, as evidenced by the steepening of the slope of the stress–strain curve [47]. Considering the modulus of human trabecular bone, which typically ranges between 10 and 3000 MPa [48, 49], our developed scaffolds showed promising results. We successfully developed UC, 10% G, 20% G, and 30% G scaffolds, which exhibited compressive moduli of 32.4 MPa, 62.5 MPa, 67.5 MPa, and 42.7 MPa, respectively. The results demonstrated a significant increase in the elastic modulus of the UCG scaffolds compared to the UC scaffold. The incorporation of 10%, 20%, and 30% PLGA into the UC composition led to remarkable improvements of 192%, 208%, and 130% in the elastic modulus, respectively. Notably, the scaffold with 20% G exhibited the highest modulus and maximum compressive strength among all compositions. PLGA is well-known for its excellent stiffness and strength characteristics. When blended with UC, PLGA contributed to the overall rigidity and load-bearing capacity of the scaffold [33]. However, it is important to note that exceeding a PLGA content of 20% in the scaffold composition resulted in a significant decrease in the elastic modulus. As previously confirmed, the UC and PLGA phases do not blend completely, resulting in phase separation. In the case of the 30% G composition, the size of the dispersed phase increased. The presence of larger phase domains can act as stress concentrators, leading to a reduction in the overall strength and stiffness of the material.

Figure 7 demonstrates the thermally triggered triple-shape memory behavior of the developed DIW-printed porous scaffold fabricated in four layers using the 10 G formulation, through a sequential programming and recovery cycle. The scaffold initially exhibited its permanent flat configuration. After heating to 70 °C, mechanical deformation followed by cooling fixed the first temporary shape (Shape A) at 45 °C, while subsequent deformation and cooling to 25 °C produced a second temporary shape (Shape B), indicating the scaffold's ability to store multiple programmed geometries. Upon reheating to 37 °C, the

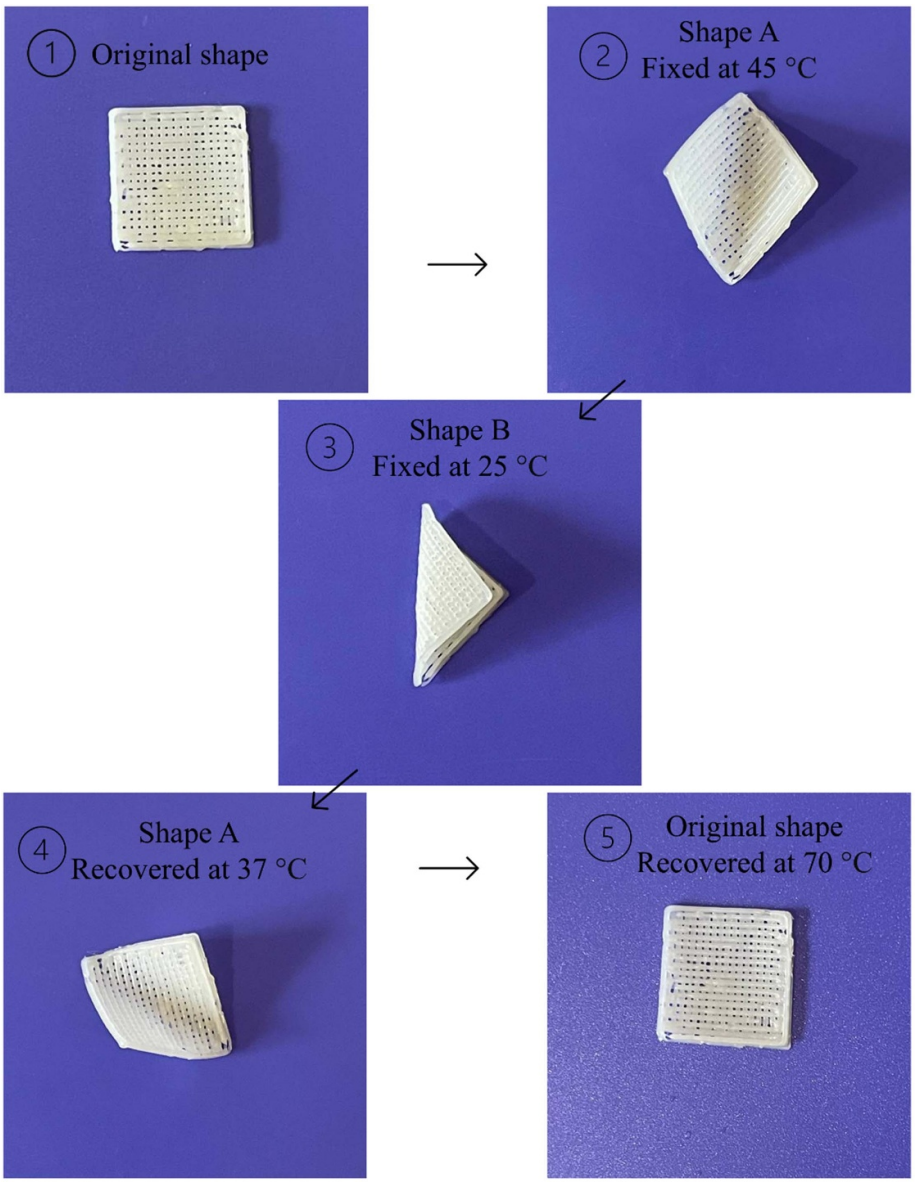

Figure 7. Demonstration of thermally induced triple-shape memory behavior of the DIW-printed scaffold. (1) Original flat shape. The scaffold was heated to 70 °C, deformed, and cooled to fix shape A at 45 °C. (2) Shape A fixed at 45 °C. Further deformation followed by cooling to 25 °C produced shape B, representing the second temporary shape. (3) Shape B fixed at 25 °C. Upon reheating to 37 °C, the scaffold recovered from shape B to shape A. (4) Shape A recovered at 37 °C. Subsequent heating to 70 °C triggered full recovery to the original permanent shape. (5) Original shape recovered at 70 °C.

scaffold recovered from shape B to shape A, demonstrating selective activation of the intermediate recovery stage, and further heating to 70 °C resulted in complete restoration of the original geometry. This multi-stage deformation and recovery sequence confirms that the developed porous scaffold possesses programmable triple-shape memory functionality at the structural level.

Notably, the printed scaffold maintained its structural integrity and interconnected porosity throughout the programming cycle, indicating that the DIW fabrication process did not compromise shape memory performance. The observed fixation of shape B at 25 °C can be attributed to the glassy state of the PLGA phase below its glass transition temperature (≈34 °C), which restricts molecular mobility and stabilizes the programmed configuration. Upon heating above the T_g, increased chain mobility within the amorphous PLGA domains enables recovery from shape B to shape A. In contrast, the fixation of shape A at 45 °C is associated with the presence of crystalline PCL domains, which remain solid below their melting temperature (≈56 °C–57 °C) and act as physical cross-links that preserve the intermediate configuration. Complete recovery of the permanent shape at 70 °C occurs when the temperature exceeds the melting temperature of PCL, allowing the release of stored elastic energy and restoration of the original geometry. These results indicate that the scaffold contains distinct thermal switching domains corresponding to the T_g of PLGA and the T_m of PCL, enabling sequential activation of shape recovery.

Such controlled multi-stage shape transformation is particularly advantageous for minimally invasive bone defect repair, where scaffolds may be introduced in compact temporary configurations and subsequently recover their functional geometry *in situ* to conform to irregular defect boundaries.

One potential approach for activating the programmed shapes of the developed scaffold *in vivo* involves localized thermal stimulation. Notably, the recovery from shape B to shape A occurs at temperatures close to physiological conditions, suggesting that partial shape recovery may be achievable at body temperature without external intervention. This characteristic is highly beneficial for minimally invasive procedures, as the scaffold could be implanted in a compact configuration and subsequently expand toward an intermediate functional shape after placement within the defect site. For activation of the permanent shape, intraoperative hot saline irrigation represents a clinically feasible strategy. Warm saline is routinely used during surgical procedures and can provide controlled thermal input while simultaneously improving the surgical field. In addition to triggering shape recovery, hot saline irrigation has been reported to offer hemostatic benefits by accelerating clot formation and reducing bleeding during and after surgery [50].

The human body can tolerate short periods of elevated local temperatures, as evidenced by the clinical use of acrylic bone cements, which can generate temperatures approaching 70 °C during polymerization [51] [52] Nevertheless, excessive thermal exposure must be avoided, as temperatures exceeding 70 °C may cause thermal injury and bone necrosis [53]. Taken together, these findings suggest that the developed scaffold could be deployed in a compact form, partially recover at physiological temperature, and achieve full restoration of its permanent geometry through controlled thermal stimulation. This programmable multi-stage recovery behavior, combined with preserved structural integrity and porosity, supports the potential suitability of the developed 4D-printed scaffold for *in vivo* bone tissue engineering applications.

3.4. Degradation characterization

The controllable degradation rate of scaffolds is a fundamental requirement in their design. Ideally, scaffolds should undergo resorption within the human body once they have fulfilled their intended function. Biodegradable polymers are prone to chemical degradation through hydrolysis or enzyme-catalyzed hydrolysis, as they contain bonds that are prone to hydrolysis.

PBS is a valuable buffer solution that closely replicates the ion concentration, osmolarity, and pH of human body fluids, making it an excellent medium for studying the degradation process of polymeric scaffolds [54]. A simple but rather effective technique to characterize the degradation of a polymeric matrix is the recording of mass loss during the degradation period. Figure 8 illustrates the quantitative and qualitative hydrolysis degradation results of UCG samples immersed in 1X PBS with a pH of 7.4 at 37 °C over a period of 16 weeks. Each week, three samples were removed from each scaffold type, washed, dried in an oven for 48 h, and their mass loss was recorded. As depicted in figure 8(a), the UC sample exhibited a relatively slow degradation rate over the entire duration of the experiment, whereas the UCG samples displayed a distinct three-stage degradation process. During the initial three weeks, the UCG compositions exhibited a relatively slow degradation rate, indicating a stable and gradual breakdown of the scaffolds (figure 8(b)). However, a notable shift occurred from weeks 4–14, specifically in the samples containing the PLGA polymer, resulting in a significant acceleration of degradation. This accelerated degradation was evident from the weight loss results at the 14-week mark, where the UC sample showed minimal weight loss (1.5%), while the 10% G, 20% G, and 30% G samples experienced substantial weight losses of 11.6%, 21.97%, and 30.51% respectively (figure 8(a)). In the final stage of degradation, during the last two weeks of the experiment, the degradation continued at a consistent rate for all UC and UCG blends, resulting in a slight increase in weight loss values to 1.6%, 11.94%, 22.1%, and 30.81% respectively. These findings are consistent with the well-established knowledge that the degradation of biodegradable polymers such as PLGA in buffer solutions follows a three-stage process.

Initially, there is a gradual decrease in both mass and molecular weight attributed to the cleavage of covalent bonds within the polymer structure. Subsequently, the degradation process experiences intermittent mass loss due to autocatalysis facilitated by carboxylic end groups, along with the significant cleavage of backbone covalent bonds. Ultimately, the degradation process culminates in complete weight loss of the polymer [55, 56]. Previous studies reported that the degradation rate of pure PLGA can be tailored from 2 weeks to 4 months depending on the ratio of its copolymers [57, 58]. Hence, our results suggest that the inclusion of degradable PLGA in UCG polymers does not exert a substantial impact on accelerating the degradation of UC component. Notably, only the PLGA component exhibited complete degradation over the course of the experiment.

We also assessed the morphological changes of the degraded samples using the SEM technique. During the initial week of incubation, all samples appeared

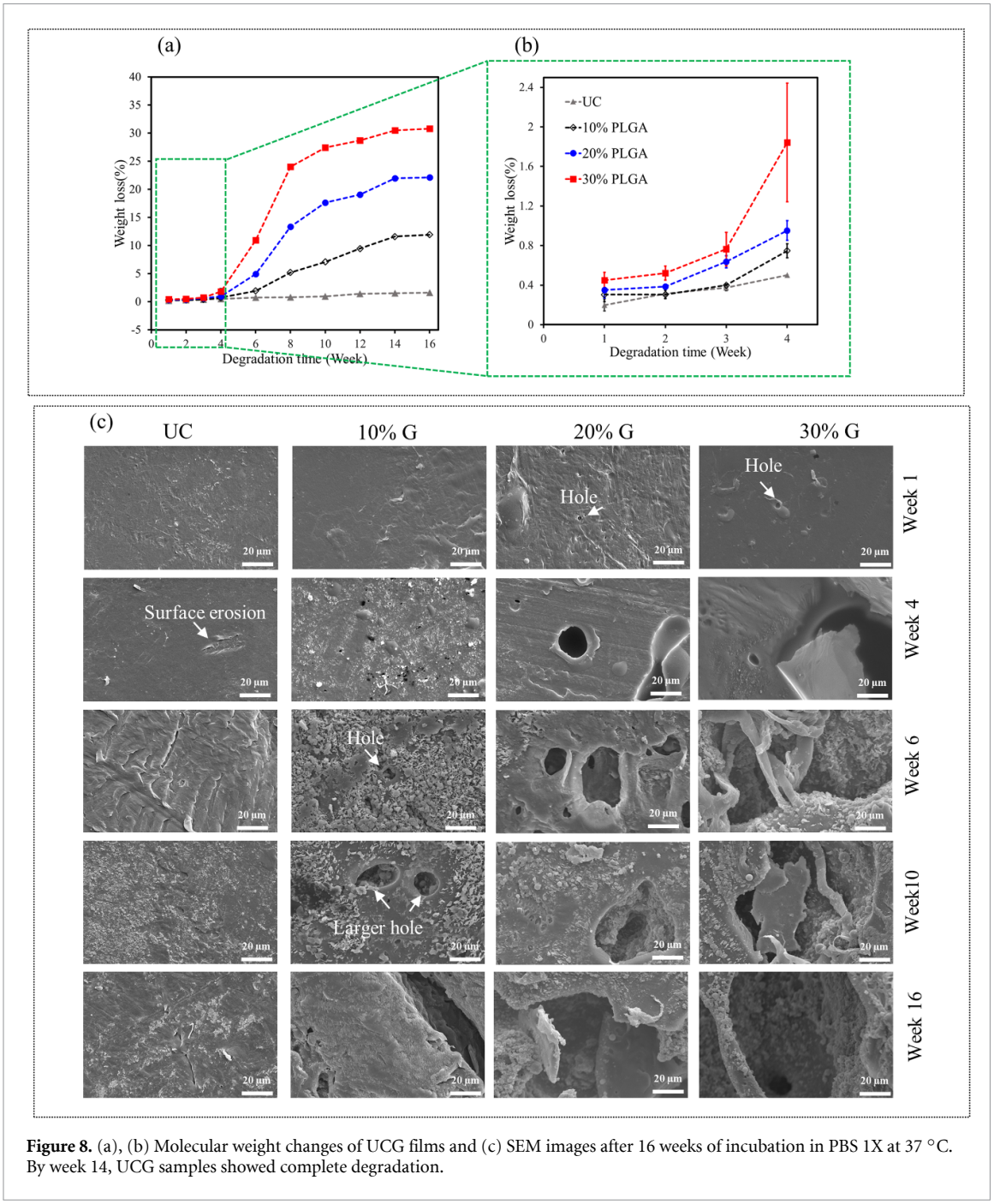

Figure 8. (a), (b) Molecular weight changes of UCG films and (c) SEM images after 16 weeks of incubation in PBS 1X at 37 °C. By week 14, UCG samples showed complete degradation.

smooth, with the presence of small holes observed on the 20% G and 30% G samples. After 4 weeks of incubation, the UC sample remained smooth, while the samples containing the PLGA component displayed an increase in the size and number of holes. By week 10, blister erosion was evident in the UC samples, and all samples showed signs of degradation, with the 30% G sample exhibiting particularly significant changes. These differences in degradation may be attributed to the higher proportion of PLGA in the 30% G sample compared to the others. In the last week of the experiment, significant morphological breakdown was observed in the 20% G and 30% G samples. These samples exhibited pronounced structural changes, indicating a more advanced stage of degradation compared to the UC and 10% G samples. The increased degradation in the 20% G and 30% G samples further supports the role of the PLGA component in influencing the degradation behavior of the scaffolds.

3.5. Cell viability

In vitro cytocompatibility studies of UC and UCG composites in 2D demonstrated cytocompatible surfaces independent of the PLGA content. The biocompatibility of all 3D printed scaffolds towards

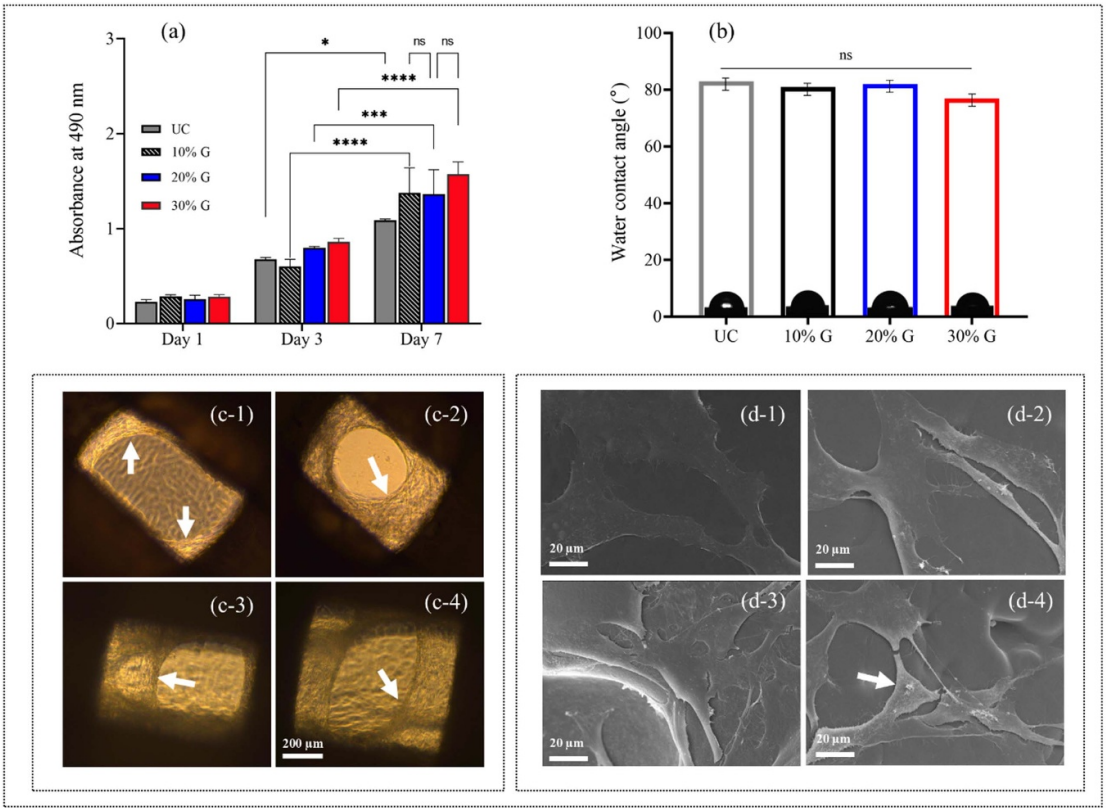

Figure 9. (a) Absorbance values from the MTS assay, (b) water contact angles of UC and UCG scaffolds, (c) optical microscopy images showing cell ingrowth on (c-1) UC, (c-2) 10% G, (c-3) 20% G, and (c-4) 30% G scaffolds after 7 d of seeding. White arrows indicate cell ingrowth and neo-tissue deposition. (d) SEM images depicting the morphology of MG-63 cells on (d-1) UC, (d-2) 10% G, (d-3) 20% G, and (d-4) 30% G scaffolds.

MG-63 cells was confirmed by the cell proliferation assay shown in figure 8. The cytotoxicity evaluation confirmed the biocompatibility of the printed UC and UCG scaffolds (figure 9(a)). On the seventh day of cell culture, no significant difference in the proliferation rate was observed between the cells cultured on 10% G, 20% G, and 30% G samples. Furthermore, all UCG scaffolds developed in this work exhibited hydrophobic surfaces, irrespective of the PLGA content (figure 9(b)). This hydrophobicity is attributed to the intrinsic properties of the PCL, TPU, and PLGA polymers used in the composition, specifically due to the presence of non-polar methyl groups. Additionally, the wettability of UC did not change upon the addition of the PLGA component. Figure 9(c) depicts cell growth inside the scaffold pores, as indicated by the white arrows, demonstrating high cell proliferation. Therefore, these scaffolds can serve as platforms for cell guidance. These findings emphasize the significance of scaffold pore design in facilitating cell sensing during the initial stages of cell adhesion and proliferation. SEM images of MG-63 cells attached and proliferated on UC, 10%G, 20%G, and 30%G scaffolds after 7 d of cell proliferation are shown in figure 9(d). The SEM images confirm that all scaffolds are suitable for cell attachment and spreading. Calcium nodules are considered a characteristic feature of osteoblast differentiation and serve as an indication of *in vitro* bone formation.

4. Conclusion

In conclusion, this study successfully developed innovative triple-SMPs using a combination of TPU, PCL, and PLGA polymers. These polymers exhibited two distinct transition temperatures, enabling the adoption of two different shapes, and achieved over 90% shape recovery ratios during two sequential recovery processes. The developed polymers were utilized for 4D DIW printing of porous scaffolds with tunable architecture, degradability, and mechanical properties. The study extensively evaluated the thermomechanical properties, morphology, and SME of the developed materials. It was observed that the incorporation of PLGA had a significant impact on the shape recovery and fixity ratios of shape B at body temperature, while it had no significant impact on the SME of shape A. Among the samples, the 10%

PLGA content exhibited the highest shape B recovery with a value of 99.5%, and the 30% PLGA content exhibited the highest shape fixity with a value of 93.7%. The developed SMPs demonstrated excellent printability, enabling successful printing at 220 °C and 200 kPa, resulting in 3D-printed scaffolds with uniform and interconnected pore distribution, ensuring structural integrity. However, it was observed that TPU/PCL/PLGA exhibited an immiscible droplet-matrix morphology, affecting the ink flowability during printing. As a result, noticeable differences in the size of struts and pores were observed among scaffolds printed using ink with different weight ratios of PLGA. Nevertheless, the DIW process was optimized to achieve scaffolds with pore sizes ranging between 352–718 μm, suitable for bone regeneration applications. Furthermore, the 4D-printed scaffolds exhibited outstanding degradability, biocompatibility, and mechanical properties comparable to human trabecular bone. It was found that the scaffold with a 20 (wt.%) PLGA content displayed the maximum mechanical properties, and exceeding this value had a negative impact on the compressive modulus. In summary, this work presents a robust and feasible approach for the 4D printing of triple shape memory bone scaffolds. These scaffolds offer a promising solution for addressing complex irregular bone defects, providing unique regenerative medicine approaches through minimally invasive surgeries.

Acknowledgments

N.S. expresses gratitude for the financial assistance received from UNSW, which includes support through a PhD research scholarship and postdoctoral writing fellowship. X.L. is the recipient of a Discovery Early Career Researcher Award (DE190101495). The authors are grateful for the scientific and technical support, as well as the facilities provided by the UNSW Mark Wainwright Analytical Centre (MWAC).

Data availability statement

The data cannot be made publicly available upon publication due to legal restrictions preventing unrestricted public distribution. The data that support the findings of this study are available upon reasonable request from the authors.

Supplementary data 1 available at: https://doi.org/10.1088/1758-5090/ae8a85/data1.

Supplementary data 2 available at: https://doi.org/10.1088/1758-5090/ae8a85/data2.

Author contributions

Nasim Sabahi
Conceptualization (lead), Data curation (lead), Formal analysis (lead), Investigation (lead), Methodology (lead), Software (lead), Validation (lead), Visualization (lead), Writing – original draft (lead)

Iman Roohani
Supervision (lead), Writing – review & editing (lead)

Kristopher A Kilian 0000-0002-8963-9796
Resources (lead), Writing – review & editing (lead)

Chun H Wang
Resources (lead), Supervision (lead), Writing – review & editing (lead)

Xiaopeng Li 0000-0003-2541-8027
Project administration (lead), Resources (lead), Supervision (lead), Writing – review & editing (lead)

References

[1] Yuan X, Zhu W, Yang Z, He N, Chen F, Han X and Zhou K 2024 Recent advances in 3D printing of smart scaffolds for bone tissue engineering and regeneration *Adv. Mater* **36** 2403641
[2] Sabahi N, Chen W, Wang C-H, Kruzic J J and Li X 2020 A review on additive manufacturing of shape-memory materials for biomedical applications *Jom* **72** 1229–53
[3] Chen X *et al* 2022 Harnessing 4D printing bioscaffolds for advanced orthopedics *Small* **18** 1–19
[4] Li Y J, Zhang F H, Liu Y J and Leng J S 2020 4D printed shape memory polymers and their structures for biomedical applications *Sci. China Technol. Sci.* **63** 545–60
[5] Lai J, Xiong T, Chen S, Zhou Z, Liu J, Yang B, Tuan R S and Li Z A 2025 Facile single-nanocomposite 4D bioprinting of dynamic hydrogel constructs with thickness-controlled gradient *Adv. Sci.* **12** 09449
[6] Chen S, Li J, Zheng L, Huang J and Wang M 2024 Biomimicking trilayer scaffolds with controlled estradiol release for uterine tissue regeneration *Exp. Physiol.* **4** 20230141
[7] Sabahi N, Roohani I, Wang C H, Farajzadeh E and Li X 2023 Thermoplastic polyurethane-based shape memory polymers with potential biomedical application: the effect of TPU soft-segment on shape memory effect and cytocompatibility *Polymer* **283** 126189
[8] Li J, Liang Z, Li T, Wan Q, Huang X and Kan Q 2025 A comprehensive review on 4D printing and applications of thermo-induced shape memory polymers *J. Biomed. Mater. Res.* **5411**
[9] Tajik E, Reihani N, Karamzadeh V, Tang G and Ravanbakhsh H 2026 Bioactive materials body-responsive shape-memory polymers for biomedical applications TEA *Bioact. Mater.* **60** 338–86
[10] Miao S, Zhu W, Castro N J, Leng J and Zhang L G 2016 Four-dimensional printing hierarchy scaffolds with highly biocompatible smart polymers for tissue engineering applications *Tissue Eng. C* **22** 952–63
[11] Hendrikson W J, Rouwkema J, Clementi F, Van Blitterswijk C A, Farè S and Moroni L 2017 Towards 4D printed scaffolds for tissue engineering: exploiting 3D shape memory

polymers to deliver time-controlled stimulus on cultured cells *Biofabrication* **9** 031001
[12] Wang Y-J, Jeng U-S and Hsu S-H 2018 Biodegradable water-based polyurethane shape memory elastomers for bone tissue engineering *ACS Biomater. Sci. Eng.* **4** 1397–406
[13] Senatov F S, Niaza K V, Zadorozhnyy M Y, Maksimkin A V, Kaloshkin S D and Estrin Y Z 2016 Mechanical properties and shape memory effect of 3D-printed PLA-based porous scaffolds *J. Mech. Behav. Biomed. Mater* **57** 139–48
[14] Senatov F S, Zadorozhnyy M Y, Niaza K V, Medvedev V V, Kaloshkin S D, Anisimova N Y, Kiselevskiy M V and Yang K-C 2017 Shape memory effect in 3D-printed scaffolds for self-fitting implants *Eur. Polym. J.* **93** 222–31
[15] Senatov F S, Niaza K V, Stepashkin A A and Kaloshkin S D 2016 Low-cycle fatigue behavior of 3D-printed PLA-based porous scaffolds *Compos. B* **97** 193–200
[16] Kutikov A B, Gurijala A and Song J 2015 Rapid prototyping amphiphilic polymer/hydroxyapatite composite scaffolds with hydration-induced self-fixation behavior *Tissue Eng. C* **21** 229–41
[17] D'amora U, Russo T, Gloria A, Rivieccio V, D'antò V, Negri G, Ambrosio L and De Santis R 2017 3D additive-manufactured nanocomposite magnetic scaffolds: effect of the application mode of a time-dependent magnetic field on hMSCs behavior *Bioact. Mater.* **2** 138–45
[18] Sabahi N, Farajzadeh E, Roohani I, Wang C H and Li X 2024 Material extrusion 3D printing of polyether-ether-ketone scaffolds based on triply periodic minimal surface designs: a numerical and experimental investigation *Appl. Mater. Today* **39** 102262
[19] Xia Y, He Y, Zhang F, Liu Y and Leng J 2021 A review of shape memory polymers and composites: mechanisms, materials, and applications *Adv. Mater* **33** 1–33
[20] Bhattacharya S, Hailstone R and Lewis C L 2020 Thermoplastic blend exhibiting shape memory-assisted self-healing functionality *ACS Appl. Mater. Interfaces* **12** 46733–42
[21] Jing X, Mi H-Y, Huang H-X and Turng L-S 2016 Shape memory thermoplastic polyurethane (TPU)/poly(ε-caprolactone) (PCL) blends as self-knotting sutures *J. Mech. Behav. Biomed. Mater* **64** 94–103
[22] Ajili S H and Ebrahimi N G 2007 Miscibility of TPU(PCL diol)/PCL blend and its effects on PCL crystallinity *Macromol. Symp.* **249** 623–7
[23] Xu X, Fan P, Ren J, Cheng Y, Ren J, Zhao J and Song R 2018 Self-healing thermoplastic polyurethane (TPU)/polycaprolactone (PCL) /multi-wall carbon nanotubes (MWCNTs) blend as shape-memory composites *Compos. Sci. Technol.* **168** 255–62
[24] Wong Y S, Xiong Y, Venkatraman S S and Boey F Y C 2008 Shape memory in un-cross-linked biodegradable polymers *J. Biomater. Sci. Polym. Ed.* **19** 175–91
[25] Baptista R and Guedes M 2021 Porosity and pore design influence on fatigue behavior of 3D printed scaffolds for trabecular bone replacement *J. Mech. Behav. Biomed. Mater* **117** 104378
[26] Peng B, Yang Y, Gu K, Amis E J and Cavicchi K A 2019 Digital light processing 3D printing of triple shape memory polymer for sequential shape shifting *ACS Mater. Lett.* **1** 410–7
[27] Tian M, Gao W, Hu J, Xu X, Ning N, Yu B and Zhang L 2020 Multidirectional triple-shape-memory polymer by tunable cross-linking and crystallization *ACS Appl. Mater. Interfaces* **12** 6426–35
[28] Liu C, Qin H and Mather P T 2007 Review of progress in shape-memory polymers *J. Mater. Chem.* **17** 1543–58
[29] Tandon B, Sabahi N, Farsi R, Kangur T and Boero G 2025 Performance comparison of shape memory polymer structures printed by fused deposition modeling and melt electrowriting **2400466** 1–12
[30] Wong Y S, Stachurski Z H and Venkatraman S S 2011 Modeling shape memory effect in uncrosslinked amorphous biodegradable polymer *Polymer* **52** 874–80
[31] Venkatraman S S, Tan L P, Joso J F D, Boey Y C F and Wang X 2006 Biodegradable stents with elastic memory *Biomaterials* **27** 1573–8
[32] Amini M and Wu S 2021 Designing a polymer blend nanocomposite with triple shape memory effects *Compos. Commun.* **23** 100564
[33] Guo H, Jiang J, Li Z, Jin Z, Hou J, Wang X and Li Q 2020 Solid-state supercritical CO_2 foaming of PCL/PLGA blends: cell opening and compression behavior *J. Polym. Environ.* **28** 1880–92
[34] Vayyaprontavida Kaliyathan A, Varghese K M, Nair A S and Thomas S 2020 Rubber–rubber blends: a critical review *Prog. Rubber, Plast. Recycl. Technol.* **36** 196–242
[35] Navarro-Baena I, Kenny J M and Peponi L 2014 Thermally-activated shape memory behaviour of bionanocomposites reinforced with cellulose nanocrystals *Cellulose* **21** 4231–46
[36] Sun Y C, Leaker B D, Lee J E, Nam R and Naguib H E 2019 Shape programming of polymeric based electrothermal actuator (ETA) via artificially induced stress relaxation *Sci. Rep.* **9** 1–12
[37] Gillispie G, Prim P, Copus J, Fisher J, Mikos A G, Yoo J J, Atala A and Lee S J 2020 Assessment methodologies for extrusion-based bioink printability *Biofabrication* **12** 022003
[38] Paxton N, Smolan W, Böck T, Melchels F, Groll J and Jungst T 2017 Proposal to assess printability of bioinks for extrusion-based bioprinting and evaluation of rheological properties governing bioprintability *Biofabrication* **9** 044107
[39] Jiang Z, Diggle B, Tan M L, Viktorova J, Bennett C W and Connal L A 2020 Extrusion 3D printing of polymeric materials with advanced properties *Adv. Sci.* **7** 1–32
[40] Zhang B, Chung S H, Barker S, Craig D, Narayan R J and Huang J 2021 Direct ink writing of polycaprolactone/polyethylene oxide based 3D constructs *Prog. Nat. Sci. Mater. Int.* **31** 180–91
[41] Schwab A, Levato R, D'este M, Piluso S, Eglin D and Malda J 2020 Printability and shape fidelity of bioinks in 3D bioprinting *Chem. Rev.* **120** 11028–55
[42] Anstey A *et al* 2021 Nanofibrillated polymer systems: design, application, and current state of the art *Prog. Polym. Sci.* **113** 101346
[43] Amini A R, Adams D J, Laurencin C T and Nukavarapu S P 2012 Optimally porous and biomechanically compatible scaffolds for large-area bone regeneration *Tissue Eng. A* **18** 1376–88
[44] Lee D J, Kwon J, Kim Y-I, Wang X, Wu T-J, Lee Y-T, Kim S, Miguez P and Ko C-C 2019 Effect of pore size in bone regeneration using polydopamine-laced hydroxyapatite collagen calcium silicate scaffolds fabricated by 3D mould printing technology *Orthod. Craniofacial Res.* **22** 127–33
[45] Ghayor C and Weber F E 2018 Osteoconductive microarchitecture of bone substitutes for bone regeneration revisited *Front. Physiol.* **9** 1–10
[46] Solomon I J, Sevvel P and Gunasekaran J 2020 A review on the various processing parameters in FDM *Mater. Today Proc.* **37** 509–14
[47] Rege A 2021 Constitutive modeling of the densification behavior in open-porous cellular solids *Materials* **14** 1–10
[48] Morgan E F, Unnikrisnan G U and Hussein A I 2018 Bone mechanical properties in healthy and diseased states *Annu. Rev. Biomed. Eng.* **20** 119–43
[49] Morgan E F and Keaveny T M 2001 Dependence of yield strain of human trabecular bone on anatomic site *J. Biomech.* **34** 569–77
[50] Sabahi N, Roohani I, Wang C H and Li X 2025 Material extrusion 3D printing of bioactive smart scaffolds for bone tissue engineering *Addit. Manuf.* **98** 104636
[51] Kim S B, Kim Y J, Yoon T L, Park S A, Cho I H, Kim E J, Kim I A and Shin J-W 2004 The characteristics of a hydroxyapatite-chitosan-PMMA bone cement *Biomaterials* **25** 5715–23

[52] Stańczyk M and Van Rietbergen B 2004 Thermal analysis of bone cement polymerisation at the cement-bone interface *J. Biomech.* **37** 1803–10
[53] Albrektsson T and Eriksson A 1985 Thermally induced bone necrosis in rabbits: relation to implant failure in humans *Clin. Orthop. Relat. Res.* **195** 311–2
[54] Ahtzaz S *et al* 2017 A study on the effect of zinc oxide and zinc peroxide nanoparticles to enhance angiogenesis-pro-angiogenic grafts for tissue regeneration applications *Mater. Des.* **132** 409–18
[55] Engineer C, Parikh J and Raval A 2011 Review on hydrolytic degradation behavior of biodegradable polymers from controlled drug delivery system *Trends Biomater. Artif. Organs* **25** 79–85
[56] Bazgir M *et al* 2021 Scaffolds for vascular tissue engineering
[57] Babilotte J, Guduric V, Nihouannen D L, Naveau A, Fricain J C and Catros S 2019 3D printed polymer–mineral composite biomaterials for bone tissue engineering: fabrication and characterization *J. Biomed. Mater. Res. B* **107** 2579–95
[58] Hutmacher D W, Schantz J T, Lam C X, Tan K C and Lim T C 2007 State of the art and future directions of scaffold-based bone engineering from a biomaterials perspective *J. Tissue Eng. Regen. Med.* **1** 245–60